Lidar temperature series in the middle atmosphere as a reference data set. Part A: Improved retrievals and a 20 year cross-validation of two co-located French lidars

Robin Wing[1], Alain Hauchecorne[1], Philippe Keckhut[1], Sophie Godin-Beekmann[1], Sergey Khaykin[1], Emily M. McCullough[2], Jean-François Mariscal[1], and Éric d'Almeida[1]

[1]LATMOS/IPSL, UVSQ Université Paris-Saclay, Sorbonne Université, CNRS, Guyancourt, France
[2]Department of Physics and Atmospheric Science, Dalhousie University, Halifax, Canada

Correspondence to: Robin Wing (robin.wing@latmos.ipsl.fr)

Abstract. The objective of this paper and its companion (Wing et al., 2018b) is to show that ground based lidar temperatures are a stable, accurate and precise dataset for use in validating satellite temperatures at high vertical resolution. Long-term lidar observations of the middle atmosphere have been conducted at the Observatoire de Haute-Provence (OHP), located in southern France (43.93° N,

5   5.71° E), since 1978. Making use of 20 years of high-quality co-located lidar measurements we have shown that lidar temperatures calculated using the Rayleigh technique at 532 nm are statistically identical to lidar temperatures calculated from the non-absorbing 355 nm channel of a Differential Absorption Lidar (DIAL) system. This result is of interest to members of the Network for the Detection of Atmospheric Composition Change (NDACC) ozone lidar community seeking to produce

10 validated temperature products. Additionally, we have addressed previously published concerns of lidar-satellite relative warm bias in comparisons of Upper Mesospheric and Lower Thermospheric (UMLT) temperature profiles. We detail a data treatment algorithm which minimizes known errors due to data selection procedures, a priori choices, and initialization parameters inherent in the lidar retrieval. Our algorithm results in a median cooling of the lidar calculated absolute temperature

15 profile by 20 K at 90 km altitude with respect to the standard OHP NDACC lidar temperature algorithm. The confidence engendered by the long-term cross-validation of two independent lidars and the improved lidar temperature dataset is exploited in (Wing et al., 2018b) for use in multi-year satellite validations.

1 Introduction

20   Rayleigh lidar remote sounding of atmospheric density is an important tool for obtaining accurate, high resolution measurements of the atmosphere in regions which are notoriously difficult to measure routinely or precisely. A key strength of this technique is the ability to retrieve an absolute temperature profile from a measured relative density profile with high spatio-temporal resolution, accuracy and precision. This kind of measurement is exactly what is required to detect longterm
25   middle atmospheric temperature trends associated with global climate change is a great value for routine satellite and model validation (Keckhut et al., 2004).

  Comparisons of middle atmospheric temperatures measured from satellites to those measured from lidars have all noted a relative warm bias in lidar temperatures above 70 km. Several recent examples of lidar-satellite relative warm bias in the upper mesosphere can be found in the work
30   of: (Kumar et al., 2003) (5-10 K relative to HALOE); (Sivakumar et al., 2011) (5-10 K relative to HALOE, 6-10 K relative to COSMIC/CHAMP, 10-16 K relative to SABER); (Yue et al., 2014) (13 K at 75 km relative to SABER); (García-Comas et al., 2014) (3-4 K at 60 km relative to SABER and MIPAS); (Yue et al., 2014) (13 K at 75 km relative to SABER); (Dou et al., 2009) (4 K at 60 km relative to SABER); (Remsberg et al., 2008) (5-10 K at 80 km relative to SABER); and (Taori
35   et al., 2012; Taori et al., 2012) (25 K near 90 km relative to SABER). The bias is generally attributed to lidar 'initialization uncertainty' and model a priori contributions to the temperature retrieval but, no systematic attempts are made to fully establish this conclusion. These authors also explore the possible influences of tides, lidar-satellite co-incidence criteria, satellite vertical averaging kernels, and satellite temperature accuracy as possible contributing factors.

40   The work of this paper is to evaluate the suitability of lidars as a reference dataset and to address the problem of systematic errors due to initialization of the lidar algorithm. The subsequent comparison of the improved lidar temperatures to satellite measurements is conducted in the companion paper (Wing et al., 2018b).

  The first part of this paper describes the current experimental setup, the specifications of two OHP
45   lidars, and the measurement cadence of two key NDACC (Network for the Detection of Atmospheric Composition Change) lidar systems.

  The second part of this paper outlines techniques to minimize the magnitude of the aforementioned lidar-satellite temperature bias by systematically detailing a rigorous procedure for the treatment and selection of raw lidar data and will propose improvements to the standard NDACC lidar temperature
50   algorithm for the UMLT (Upper Mesosphere and Lower Thermospshere) region.

  The third part of this paper compares the lidar temperatures produced by an NDACC certified temperature lidar at 532 nm with temperatures produced by the non-absorbing 355 nm line of a co-located NDACC certified ozone DIAL (DIfferential Absorption Lidar) system. This comparison is conducted using a large database of two co-located lidar systems with the goal of providing con-
55   fidence in the longterm stability of the lidar technique at both wavelengths. There are currently 10

certified temperature lidars, 6 of which are current in their data submission and have temperature profiles freely accessible online. Similarly, there are 12 certified stratospheric ozone DIAL systems of which 5 systems are current with data submission and are available through the NDACC website. We hope that this work will encourage sites with outstanding data obligations to submit their

60   measurements and for DIAL ozone sites to seek validation for their temperature data products for inclusion in the NDACC database (nda). As an ancillary goal we will show that temperatures produced by the Rayleigh lidar technique are accurate, precise and stable over multiple decades and as such are the ideal type of measurement for use in future ground based validation of satellite temperatures. The result of this demonstration will be used in the companion paper (Wing et al., 2018b) as

65   justification for validating satellite data with lidar temperatures.

2   Instrumentation Description

2.1   Rayleigh Lidar

The OHP Rayleigh-Mie-Raman lidar, LTA (Lidar Température et Aérosols), uses a seeded Nd:YAG to produce a 532 nm laser source with a maximum power of 24 W. The transmitted beam is passed

70   through a 13X beam expander and has a 30 Hz repetition rate, a 7 ns pulse width, and a beam divergence of less than 0.1 mrad.

The receiver assembly consists of a high and low gain elastic channel for 532 nm, a Mie scatter channel for aerosols, a Raman channel at 607 nm for molecular nitrogen, and a Raman channel at 660 nm for water vapour. A schematic of the telescope array is shown in Fig. 1. The high gain

75   Rayleigh channel consists of four telescopes. At the focal point of each telescope is an actuator-mounted 400 μm diameter fibre optic. The four fibre optics are bundled to project a single signal onto a Hamamatsu R9880U-110 photomultiplier. The low gain Rayleigh, nitrogen Raman, water vapour Raman and Mie channels all use a single telescope setup and actuator mounted fibre optic. The two Raman channels rely on the largest telescope and the signals are separated by a dichroic

80   mirror. Specifications for each telescope are found in Table 1.

LTA	Mirror Diameter (mm)	Focal Length (mm)	Field of View (mrad)	Parallax (mm)	Optical Filter Width (nm)	Filter Maximum Transmission (%)
High Gain Rayleigh	4X 50	1500	0.27	800	0.3	84
Low Gain Rayleigh	20	600-800	1.7	257	0.3	84
Nitrogen Raman	80	2400	0.6	600	1	∼ 50
Water Raman	80	2400	0.6	600	1	∼ 50
Aerosol Mie	20	600-800	1.7	257	0.3	84

Table 1: Specifications for the LTA receiver assembly.

All channels are sampled using a Licel digital transient recorder with a record time of 0.1 μs which corresponds to a vertical resolution of 15 m. The high and low gain Raleigh channels are electronically gated at 22 km and 12 km, respectively, to avoid damaging the photomultipliers with large signal returns. Further details can be found in (Keckhut et al., 1993).
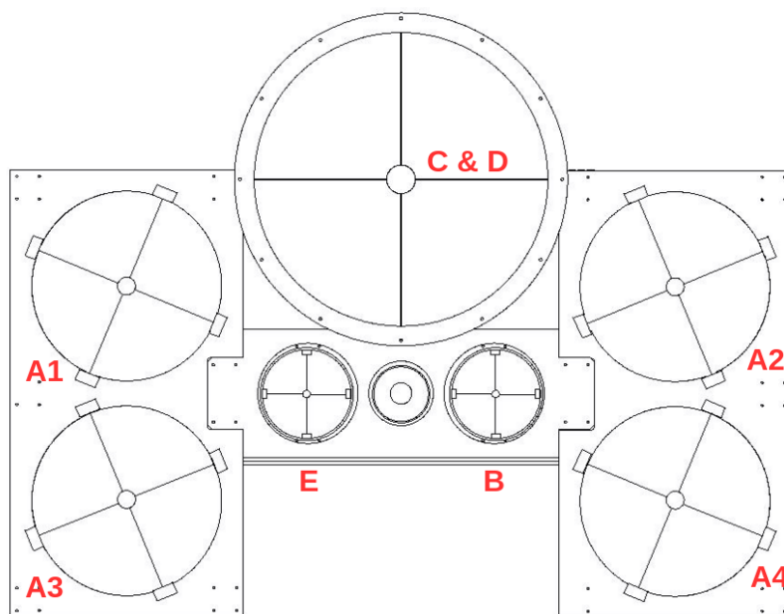
Figure 1: Mirrors A1, A2, A3, A4 (50 cm) are combined for the high gain Rayleigh channel. B (20 cm) is low gain Rayleigh channel. Mirror C&D (80 cm) is the Raman channel for water vapour and molecular nitrogen. E (20 cm) is the Mie channel. The beam expander for the transmitted laser source is between mirrors E and B.

2.2 DIAL Ozone System (LiO$_3$S)

85

The OHP Differential Absorption Lidar (DIAL) uses two lasers to make a measurement of the vertical ozone profile using the differential absorption by ozone at two different wavelengths. The first laser is an XeCl eximer laser used to produce a 308 nm laser source with a maximum power of 10 W. The beam is passed through a 3X beam expander and has a final divergence of less than 0.1 mrad. The second laser is a tripled Nd:YAG which is used to produce a 355 nm laser source with a maximum power of 2.5 W. The beam is passed through a 2.5X beam expander and has a final divergence of less than 0.2 mrad. Both transmitted beams have a repetition rate of 50 Hz, and a 7 ns pulse width.

90

The receiver assembly consists of four 530 mm mirrors each having a focal length of 1500 mm, a field of view of 0.67 mrad, and an average parallax of 3100 mm. Each of these four telescopes

95

are focused onto an actuator-mounted 1 mm diameter fibre optic. The outgoing signals are bundled before being passed through a mechanical signal chopper to block low altitude returns below 8 km which would saturate the photon counting electronics. The combined signal is split using a Horiba Jobin Yvon holographic grating with 3600 grooves/mm and a dispersion of 0.3 mm/mm. The light

100 from the grating is projected directly onto the photomultipliers for a high (92%) and low gain (8%) Rayleigh channel at 308 nm, a high gain (92%) and low gain (8%) Rayleigh channel at 355 nm, and two Raman channels at 331.8 nm and 386.7 nm for molecular nitrogen. The spectral resolution of the light incident on the photo cathode is on the order of 1 nm. Figure 2 shows a schematic of the OHP DIAL system.

105 All channels are sampled using a Licel digital transient recorder with a record time of 0.25 μs which corresponds to a vertical resolution of 75 m. Further details can be found in (Godin-Beekmann et al., 2003).
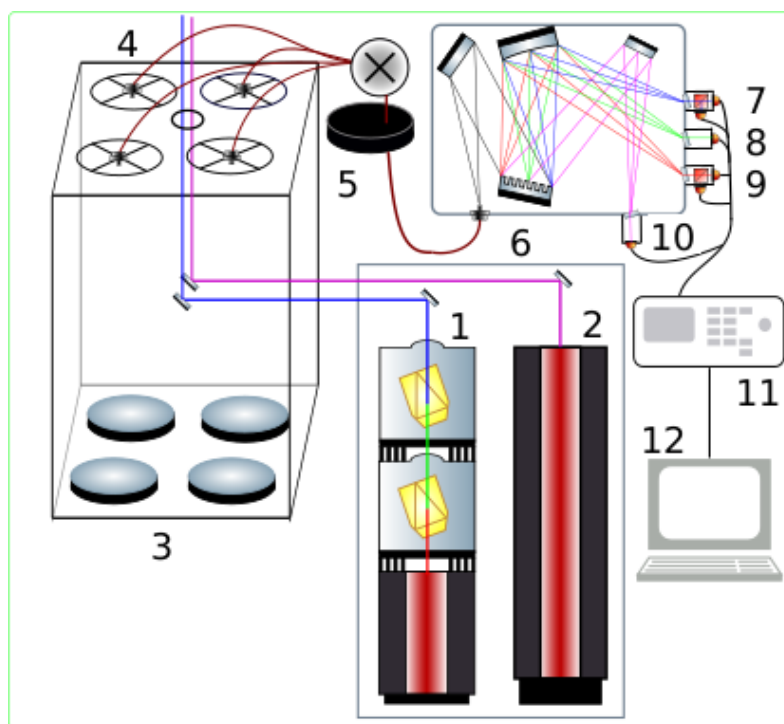
Figure 2: LiO$_3$S DIAL system. **1** 355 nm laser source, **2** 308 nm laser source, **3** four 530 mm mirrors, **4** four actuator mounted fibre optic cables, **5** mechanical chopper, **6** Horiba Jobin Yvon holographic grating, **7** 308 nm high and low gain photomultipliers, **8** 331.8 nm photomultiplier, **9** 355 nm high and low gain photomultipliers, **10** 386.7 nm photomultiplier, **11** Licel transient signal recorder, **12** Signal processing and analysis computer.

3 Methods

In this section we will set forth rigorous and well defined procedures for the retrieval of lidar tem-
peratures in the middle atmosphere which will minimize the uncertainties at the upper limit of the
lidar altitude range.

3.1 Rayleigh Lidar Equation

To calculate absolute temperature profiles from relative density profiles we exploit the gradient of
the measured profile of back-scattered photons collected by the receiver. From classical lidar theory
(Hauchecorne and Chanin, 1980), we know that the number of photons received is a simple product
of transmitted laser power, atmospheric transmission, telescope geometry, and receiver efficiencies.
This quantity can be expressed numerically in Eq. (1):

$$N(z) = \xi_{sys} \cdot \tau_{emitted}(z,\lambda) \cdot \tau_{return}(z,\lambda) \cdot O(z) \cdot P_{laser} \cdot \beta_{cross} \cdot n(z) \cdot \frac{A}{4\pi z^2} \cdot \Delta t \cdot \Delta z + B$$

(1)

N is the count rate of returned photons per time integration per altitude bin

z is altitude above the detector

ξ_{sys} is the system specific receiver efficiency

$\tau_{emitted}(z,\lambda)$ is the transmittance of the photons through the atmosphere

$\tau_{return}(z,\lambda)$ is the return transmittance of the photons through the atmosphere

$O(z)$ is the overlap function of the receiver field of view

P_{laser} is the laser power at a given wavelength

β_{cross} is the backscattering cross section of the target molecule

$n(z)$ is the number density of scatterers in the atmosphere

$\frac{A}{4\pi z^2}$ is the effective area of the primary telescope

Δt is the temporal integration for data collection

Δz is the spatial range over which photons in a bin are integrated

B is the background count rate.

There are four simple assumptions we make when Eq. (1) is used. First, we assume that each
photon we count only scatters once. While this is almost certainly not the case, we can say that it
is approximately true. Visual wavelength photons have a very low probability of scattering in the
atmosphere and with a multiple-scatter process we must square that very small probability. Of these
multiply scattered photons, only those with a scatter angle towards the lidar receiver assembly will
be seen with the vast majority scattering outside out field of view. Further, the tenuous nature of the
UMLT means that the small probability of detecting a photon which has scattered more than once
becomes exponentially negligible with increasing altitude.

Second, we assume that the atmospheric density is directly proportional to the number of re-
turned photons incident on the receiver assembly. In the case of high signal returns from the lower

atmosphere, when the number of returned photons can saturate the photon counting electronics, the measured photon count rate will diverge from the received photon count rate. Multiple detection channels, at different sensitivities, are used to compensate for this effect. In this work we are primarily concerned with the UMLT, a region where lidars operate at very low count rates, so for the purposes of this work we can safely make this assumption.

Third, we assume that the atmosphere is in local hydrostatic equilibrium as well as local thermodynamic equilibrium (LTE) and obeys the ideal gas law. This assumption is potentially problematic at high altitudes where non-LTE processes can affect gravity wave dynamics and temperature profiles (Apruzese et al., 1984). In this work we are unable to relax this assumption.

Fourth, we assume that the atmosphere is generally free of aerosols above 30 km and the lidar returns above this height are solely due to Rayleigh scattering processes (Hauchecorne and Chanin, 1980).

In the UMLT the signal to noise ratio and the model derived a priori assumptions for pressure and density are the main sources of error for the lidar temperature retrieval method. This paper lays out a rigorous method for reducing the noise in this region of the lidar signal with the goal of producing more robust mesospheric temperatures.

3.2 The Raw Counts Lidar Signal

When backscattered photons are incident on the lidar receiver they are co-added for a set period of time in the counting electronics. This ensures that the recorded signals are based on a similar number of transmitted photons. In the case of LTA a photon count profile, as a function of arrival time, is generated for every 5000 laser shots. Similarly for LiO_3S a photon counts profile is produced for every 8000 laser shots. These measurements can be further co-added for the entire night to increase the signal to noise ratio at the upper limit of the measurement range. We use the speed of light to convert our profiles of photon count rate per second as a function of arrival time at the detector to total photon count rate per second as a function of altitude.
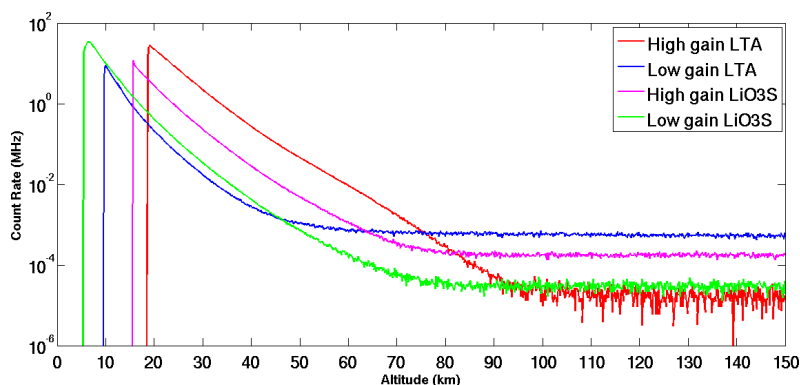
Figure 3: Nightly co-added scans for high and low gain Rayleigh signals for LTA and LiO$_3$S. The background for LTA extends to 246.23 km and for LiO$_3$S extends to 154.13 km. A single lidar scan for both LTA and LiO$_3$S has a temporal resolution of roughly 2 minutes and 45 seconds and a vertical resolution of 7.5 m.

Figure 3 shows four nightly co-added OHP lidar count rate profiles as a function of altitude. Both lidar systems employ a high gain and a low gain channel to extend the measurements over a greater altitude range. The lower altitudes (corresponding to the fastest signal return times) of each channel are either blocked by a mechanical chopper or electronically blanked. This is done to avoid saturation of the receiver assembly from very large signals in the lower atmosphere. Additionally, each channel has a set of optics designed to minimize the noise, with greater care being given to the high gain channels. These optics are fully described in the instruments Sect. 2.

3.3 Identifying Outliers, Signal Spikes, Signal Induced Noise, and Transient Electronic Interference

When retrieving lidar temperature profiles in the UMLT it is necessary to take extra precautions to carefully remove outliers, spikes, and electronic contamination from each profile in both the background region and the signal regions. Any contamination of the signal in the background region will be of the same order of magnitude as the true signal and thus, have a disproportionate effect on the temperature. An overestimation of the noise will result in the removal of true photons, a lower estimated density, and by the ideal gas law, a warmer temperature. The opposite holds true for an underestimation of the background (produces a colder profile). The shape of the temperature profile itself will be distorted if there is a non-constant background. If it is not possible to fully correct the issue it is highly recommended to exclude the entire scan from the nightly analysis.

3.3.1 Spikes

Spikes in fast integration photon counting data are not always easy to spot but can be defined as anomalously large, isolated, signal rates which occur in only one altitude bin without affecting adjacent data. If not properly identified and extracted from the data they can contribute to false temperature features and inaccurate background estimations. It is particularly challenging to separate small amplitude spikes when the signal to noise approaches 1. It is therefore necessary to establish a consistent criterion to determine which data points belong to the the population of real lidar returns and which points are likely contamination spikes. We have chosen to employ a straight forward Tukey Quartile test on the difference between consecutively binned lidar returns as this statistic is relatively insensitive to signal drift during the course of the night. The quartile technique is equally useful in both regions of high signal returns as well as the background regions and shows stability and consistency in identifying outliers. Figure 4 is a plot of photon count rate as a function of binned arrival time and shows an example of several photon count acquisitions plotted as a stack plot with the black line representing the 2σ limit on the population of lidar returns. Data points above the black line are considered as signal contamination and are removed from the analysis.
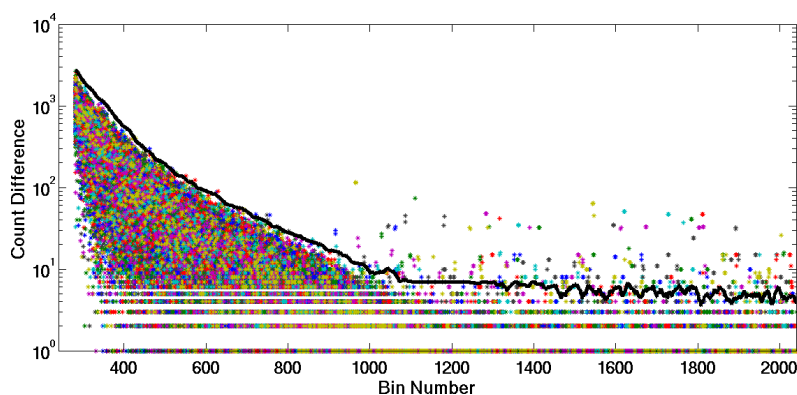
Figure 4: Tukey Quartile spike identification based on the signal difference between consecutive lidar time bins for short integration lidar returns. An entire night of lidar scans is over-plotted in the stack plot. The black line is the 2 sigma limit and points above this line are removed.

3.3.2 Transient Electronic Signals

Transient Electronic Signals (TES) are short lived bursts in the lidar acquisition chain and may be internal to the system or related to nearby electronic interference. Possible sources for these transients include photomultiplier ringing from signal saturation, voltage fluctuations in the power supply, ambient RF signals, and ground loops between lidar electronics and Ethernet switches with

205 metal sheathed cables. While these events are rare they can drastically alter the background and resulting temperature profile by inducing wavelike structures into the data.

Unlike simple spikes these features have an amplitude, a duration, and an effect on the downstream counting rate. In the example shown in Fig. 5 (top) is a surface plot of counts differences between consecutive bins for the first 100 bins of lidar data. This plot shows scans for a night of lidar data with

210 each scan accounting for roughly 1.6 minutes of lidar data. We can see that the 22nd and 46th scans are contaminated by a TES with a duration of about 0.5 μs. These signals cannot be detected using the Tukey Quartile test as the time derivative of the photon return signal may not be sufficiently far from the nightly population median. However, a 2-D kurtosis test will consistently detect this type of signal contamination as a TES will induce a large skew in the photon count rate population

215 distribution. The kurtosis test is done in the time dimension as well as with altitude to exclude false positives in the photon count rate skew which may be due to clouds or aerosols. Figure 5 (bottom) shows a plot of the kurtosis in the population of photon counts in each lidar scan and the red line shows the 2σ estimation of total lidar scan skew. Isolated scans with a total kurtosis above this limit are excluded.
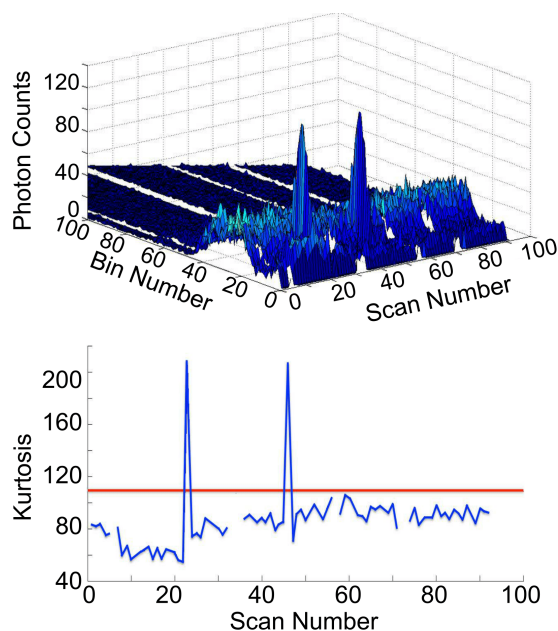
Figure 5: Upper panel is a surface plot of lidar returns as a function of time bin and scan number. Two instances of TES can be seen as anomalous peaks in the photon count rate. Lower panel is a summation of the fourth statistical moment (kurtosis/skew) for each scan. The red line indicates a 2σ limit on the skew of the population. Points above the limit are excluded.

3.3.3 Bad Scans

After the removal of lidar scans which suffer from clear signal contamination, there may still be scans which ought not be included in a lidar temperature analysis. Conceptually, 'bad scans' are lidar scans with a high background and/or a low signal strength. These scans need to be positively identified as not belonging to the general population of nightly lidar scans and excluded. Quantitatively, identifying a 'bad scan' is a challenge as both the background and the signal can change abruptly over the night as the laser power drops or sky conditions change (see Fig. 6 for an example). In the top panel of the figure we see the evolution of the background for a night of lidar data. Intuitively, we might suggest that scans 1 through 23 and scans 36 through 46 might belong to one population and the rest (excluding scan 69) belong to a second population. However, when we look at the panel representing the signal our intuition becomes a bit more subjective. There are clearly four groups of similar signals which match fairly well with the changes in the backgrounds shown in the panels above however, whether these four groups of signals represent two, three, or four distinct populations is somewhat dependent on which statistics the author chooses to use.

We have shown two approaches for attempting to address the issue of changing signal quality. Both have advantages and points for concern and illustrate just how subtle and challenging this aspect of lidar science can be. In Fig. 6 the green margin is an attempt to identify 'bad scans' based on a moving average approach however, this method cannot accommodate quick transitions in signal strength and results in false positives when signal quality changes abruptly. The blue line is an attempt to use Matlab Neural Network software to estimate the number of lidar signal-to-noise populations for a given night. This approach was abandoned as the training process for the software requires an exhaustive set list of example 'bad profiles' which we cannot supply. Additionally, we found that estimating the number of local medians for each sub-population of lidar scans in a given night was too highly dependent on the number of degrees of freedom specified in the Matlab tool.
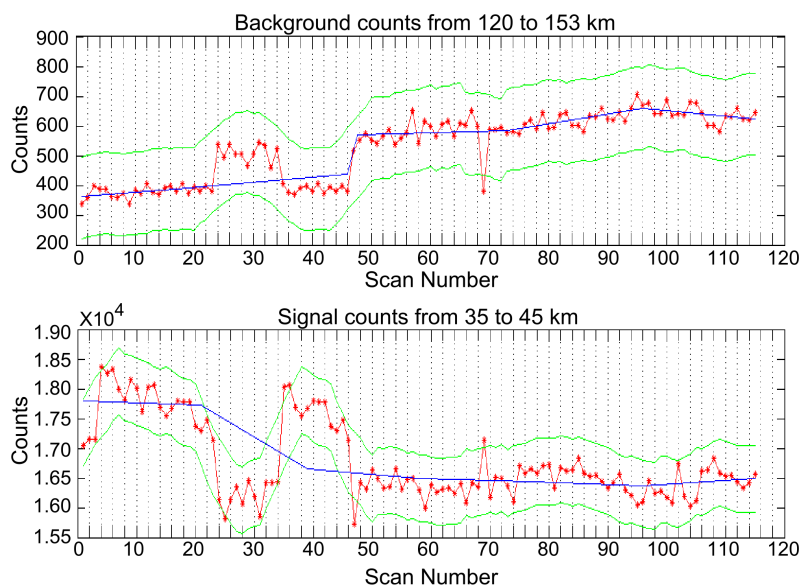
Figure 6: Example of lidar signal and noise during a night of measurements. Top panel shows the total background counts summed from 120 km to 153 km and the bottom panel shows the total signal summed between 35 km and 40 km. Green bounds are calculated based on a simple moving average of the counts (red) and the blue line is an attempt to estimate local population medians using the Matlab Neural Network tool.

The simple reality of ground based observation means that lidar signals clearly detect changes in
245 the viewing conditions such as moonrise, thin cirrus clouds, optically thick clouds, changing light
pollution, as well as changes in signal quality. Systematically identifying outlier signals is further
complicated as there can be multiple signal to noise population medians during the course of the
night. To properly characterize the non-Gaussian distribution of scans and determine which should
be excluded requires a non-parametric statistic. We use a one sided non-parametric Mann-Whitney-
250 Wilcoxon rank-sum test to identify lidar scans which do not belong to the nightly population or
subpopulations of lidar scans.
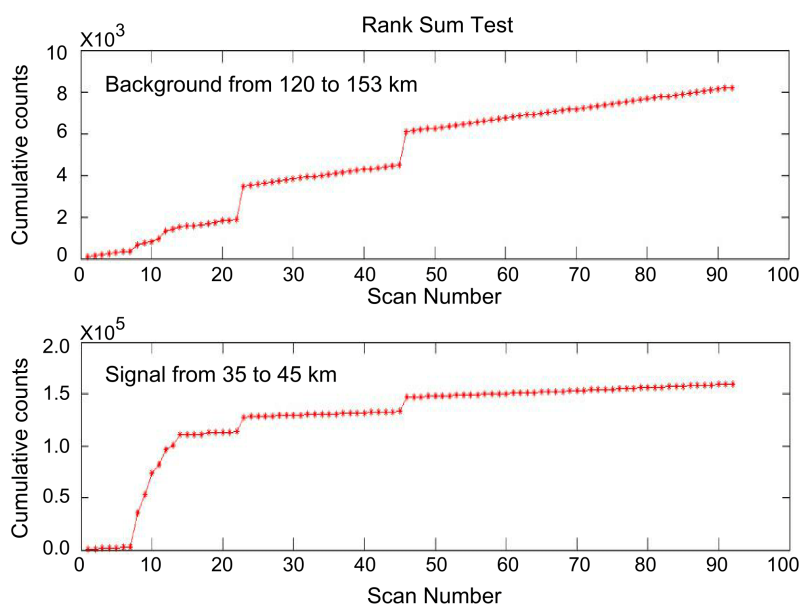
Figure 7: Rank sum plots for a night of lidar data. Top panel is the cumulative background count and the bottom panel is the cumulative signal count. The signal to noise ratio of the rank summed photon counts in each profile is evaluated using a Mann-Whitney-Wilcoxon rank-sum test to determine if an individual lidar scan belongs to the nightly population of lidar scans.

Figure 7 shows the ranked sum of the background (noise) and signal counts for a night of lidar data. We do not exclude the profiles which fail the test for having high quality. The benefit of using this metric is that it allows us to have a standardized definition of a 'bad scan' which takes into account the nightly median without the assumption that the quality of lidar scans is normally distributed. In this example the first 13 scans fail the rank-sum test and are discarded.

3.3.4 Good Scans

Given that our objective is to calculate accurate temperature profiles at the highest possible altitudes we must quality test each scan that we choose to include in the nightly average. It is possible to include partial scans but that is not done in this work. The conceptual difference between a 'bad scan' and a 'good scan' is that bad scans are positively identified as outliers to the general population whereas good scans represent the portion of the population of scans which contribute more information than noise to the nightly average at a given altitude. Consider that a poor quality lidar scan which has a signal to noise ratio of 1 at 70 km contributes more information than noise at 60 km, but more noise than signal at 80 km. Thus, we need a flexible metric to determine signal quality over a diagnostic altitude which reflects the general signal quality of the night.

Quantitatively, we express this with a signal, S, to noise, N, inequality in Eq. (2). The noise is always evaluated between 120 km and 155 km and the altitude range for the evaluating the signal is defined as the scale height below the point where the signal to noise equals one in the density profile. Each individual scan has a value representing the signal, S_i, and a noise, N_i. The scan values are compared to the nightly sum of the signal, S_{sum} and the nightly sum of the noise, N_{sum}. If a scan fails the inequality test then it is not included in further nightly analysis.

$$\sqrt{\frac{S_{sum} + N_{sum}}{S_{sum}}} < \sqrt{\frac{(S_{sum} - S_i) + (N_{sum} - N_i)}{S_{sum} - S_i}} \tag{2}$$

3.4 Noise Reduction

Statistical uncertainty in photon counting can be described by a Poisson distribution based on the square root of the number of photons received. Systematic uncertainties in the photon counts are introduced by ambient background light (light pollution, moonlight etc.), thermal excitation in the photomultipliers (so-called dark current), and signal induced noise. The first two sources of error are minimized by using narrow filters in the optical receiver chain and by cooling the photomultipliers. The signal induced noise can be very difficult to correct experimentally and is usually estimated in data processing. This type of noise can occur if the photomultipliers have become saturated at any point in the signal acquisition process and often manifest as non-linear artifacts superimposed upon the true photon count profile.

Figure 8 shows the reduction in the background noise due to recent hardware improvements. The first drop corresponds improvements made to the photomultiplier cooling system which reduces the number of thermally excited electrons detected at the photo cathode of the photomultiplier in the absence of signal from the sky. The second drop in background counts results from replacing the Hamamatsu R7600U-20 multi-alkali photomultiplier with the improved Hamamatsu R9880U-110 photomultiplier having a super bi-alkali photo-cathode. The third and final drop in background counts is a result of replacing a 532 nm optical filter which has a width of 1 nm with a newer filter having a bandwidth of 0.3 nm. These experimental modifications result in a 100 fold decrease in the background noise and allows us greater confidence in our UMLT temperature retrievals. The regular monthly variations in the signal which become apparent at lower noise levels are due to the phase of the moon.
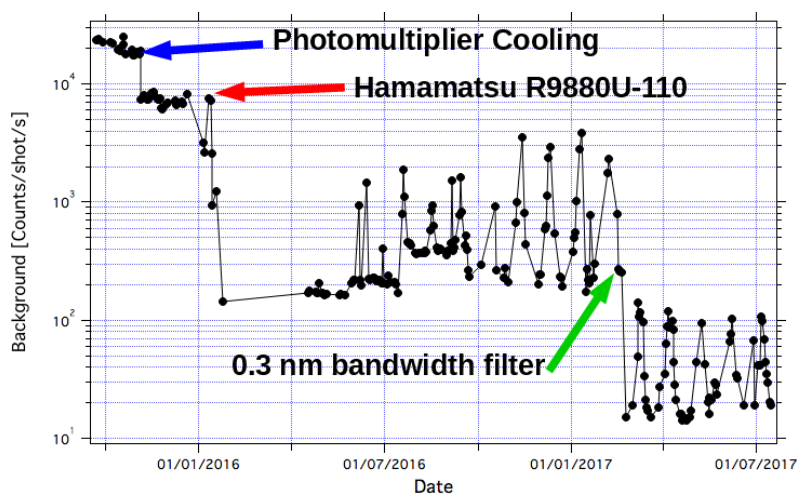
Figure 8: This figure shows the improvements in the background count rate due to photomultiplier cooling, new photomultipliers, and new optical filters. Note the logarithmic y-axis and the total reduction of background counts by more than 2 orders of magnitude.

3.5 Corrections Applied Before Temperature Calculation

In the previous subsection we detailed the process for removing bad scans from our nightly lidar measurement. In this subsection we will detail several corrections to our remaining photon counts profiles which correct for signal saturation, atmospheric transmission, and background estimation.

3.5.1 Deadtime Correction

The OHP lidars measure photons using photomultipliers and a digitizing signal counter. This system is highly efficient at detecting low signals and is optimized for single photon returns in the UMLT. However, given that the returned lidar signal directly follows the exponential density of the atmosphere, the photomultipliers and counting systems are susceptible to missing photons at lower altitudes due to high count rates. To correct for this saturation effect we can estimate a correction coefficient, τ, also referred to as a deadtime. The background theory and derivation of Eq. (3) is well described by (Donovan et al., 1993), where N is the photon count rate and Δt is the measurement time interval. This deadtime correction can be calculated based on factory specification of the counting electronics, a theoretically derived deadtime, or it can be measured directly using a low gain lidar channel. The OHP lidars measure the deadtime directly and correct for saturation in the high gain channels with information from the low gain channels. If the low gain channel is not available a theoretical correction of 7 ns is applied to pre-2013 data and 4 ns is applied to more recent data following the installation of a Licel digital recorder.

$$N_{counted} = N_{received} * exp(\frac{\tau * N_{received}}{\Delta t})$$ (3)

3.5.2 Atmospheric Transmission Correction

315   To correct for Rayleigh extinction we use MSIS-90 model (Picone et al., 2002) to generate a vertical
profile of ozone, molecular oxygen, oxygen radical, molecular nitrogen, and argon, and then apply
the correct Rayleigh cross-section to each species. This method is adapted from (Argall, 2007) and
is important for accurate retrievals of density and neutral temperature in the UMLT. Correction for
aerosols is not done in this work as we assume that the atmosphere is generally clean above 30 km
320   (Hauchecorne and Chanin, 1980).

3.5.3 Defining the Background

Normally, we assume that the rate of counted photons per laser shot is constant in the background
region during the signal acquisition time and can therefore be approximated by a simple Poisson
distribution. We further assume that in this background region we are not measuring returned photons
325   from the laser signal but instead are measuring ambient sky light. However, if there is a non-linear
signal induced noise in the photon counting chain, the number of counted photons is not constant
with time during the acquisition period of a single laser shot. When this occurs we cannot assume
that the variation in the background is a strictly Poisson distribution around a constant expected
value.

330   If left uncorrected, we risk overestimating the number of 'true' photons returned from the upper
atmosphere and the result is an artificially dense and cold UMLT. Erring on the side of caution we
fit three backgrounds (constant, linear, and quadratic) to each nightly summed profile, in a standard
diagnostic region, and choose the function with the best Chi-squared goodness of fit as our estimate
of signal induced noise. Shown in Fig. 9 is an example of a night where the low gain Rayleigh chan-
335   nel (blue) experienced signal induced noise which was best approximated by a quadratic function;
the high gain Rayleigh channel (red) had a background best estimated by a small negative linear
function; and the nitrogen Raman channel (green) had no apparent signal induced noise and was fit
with a constant background. The optimal solution for non-linear signal induced noise is to determine
the contribution of both the signal and the noise using exponential fits however, we have found that
340   method to be extremely sensitive to the choice of background diagnostic region and was less stable
than the simple quadratic approximation. Our standard altitude range for background selection is 120
km to 155 km but this number is system and channel specific. To illustrate this point we compare the
background regions of the high gain Rayleigh channel (red) and the nitrogen Raman channel (green)
in Fig. 9. The nitrogen Raman channel background could be calculated from 50 km to 155 km or
345   120 km to 155 km and yield the same result.
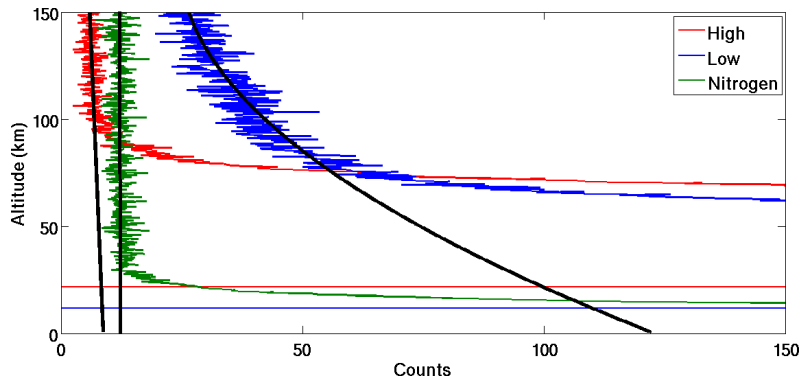
Figure 9: An example of a non-linear signal induced noise in the low gain Rayleigh channel best estimated by a quadratic background. Also shown is the high gain Rayleigh channel (red) with a background best fit by a negative linear function and the nitrogen Raman channel (green) with no apparent signal induced noise and a constant background.

3.6 Temperature Inversion Equation

The standard NDACC algorithm for Rayleigh temperature retrieval is the Hauchecorne-Chanin (HC) method (Hauchecorne and Chanin, 1980) which makes a scalar normalisation of the photon-count profile to an in-situ density measurement or to a density calculated from a model like CIRA-72, SPARC-80, or MSIS-90. From a density gradient profile we calculate a pressure gradient profile Eq. (4) and using the ideal gas law, Eq. (5), we can arrive at an expression for pressure, Eq. (6). Here P is pressure, z is altitude above the lidar station, ρ is density, g is the latitude dependent acceleration due to gravity for an ellipsoid Earth given by the Somigliana formula, R is the ideal gas constant, T is the temperature, and M is the molecular mass.

$$dP(z) = -\rho(z)g(z)dz \tag{4}$$

$$P(z) = \frac{R\rho(z)T(z)}{M} \tag{5}$$

$$\frac{dP(z)}{P(z)} = -\frac{Mg(z)}{RT(z)}dz = d(\log(P(z))) \tag{6}$$

The crux of the challenge for initializing the lidar equation lies in the non-linear nature of Eq. (6) which will necessitate the introduction of an a priori estimate of pressure at the top of the atmosphere followed by an iterative approach to retrieving the profile at lower attitudes. A full theoretical description of this problem was well laid out by (Khanna et al., 2012). In this work we have chosen to take our initial a priori seed pressure value, $P(z_1)$, from the MSIS-90 model. We now arrive at an iterative expression for the generation of the pressure profile as a function of altitude Eq. (7).

$$\frac{P(z_i) - \frac{\Delta z}{2}}{P(z_i) + \frac{\Delta z}{2}} = \exp\frac{Mg(z_i)}{RT(z_i)}\Delta z \tag{7}$$

365   Given our iteratively generated pressure profile we can do an inverse calculation to map our pressures to a set of temperatures using Eq. (8) and Eq. (9). This iteration starts at the top of the atmosphere, in an area low signal to noise and thus of large relative uncertainty, and proceeds downwards in altitude and becomes exponentially less uncertain with each step as signal quality improves with increasing atmospheric pressure. As we iterate downward the influence of our choice of a priori pres-

370 sure becomes less significant and the calculated temperature profile becomes entirely data driven.

$$X_i = \frac{\rho(z_i)g(z_i)\Delta z}{P(z_i) + \frac{\Delta z}{2}} \quad (8)$$

$$T(z_i) = \frac{Mg(z_i)}{R\log(1 + X_i)}\Delta z \quad (9)$$

    In order to calculate a single temperature profile from 5 km to above 80 km we meld the photon counts from the high and low gain Rayleigh channels together with the counts from the N_2 Raman

375 channel. The slope of the logarithm of each of the three photon counts profiles is compared to a synthetic lidar counts profile generated based on the nightly average MSIS-90 density profile. The comparison gives us a first estimation of the linearity and alignment of the lidar data. We then select a clear linear region of each scan to use in calculating a MSIS derived scaling factor for each profile. This procedure allows the top of the nitrogen Raman profile to be melded to the bottom of the low

380 gain Rayleigh profile and the top of the low gain Rayleigh profile to be melded to the bottom of the high gain Rayleigh profile. The melding calculation is conducted over a signal-to-noise defined altitude range and is a straightforward weighted average. The resulting melded density and pressure profiles are used to generate a single temperature profile like the one shown in Fig. 10. The use of MSIS-90 as a scalar density reference for the synthetic lidar profile does not affect the final lidar

385 temperature profile which depends only on the relative density and not the absolute value. We follow similar procedures to those described by (Alpers et al., 2004).
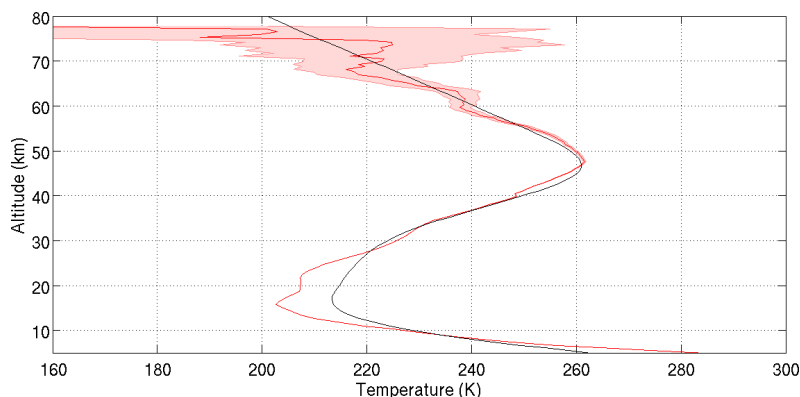
Figure 10: An example of a melded temperature profile from two Rayleigh channels and one Raman channel. The profile is calculated at 300 m vertical resolution from a single combined photon count profile and has a maximum relative error near 80 km of 30%. Black line is the MSIS-90 temperature profile which corresponds to the MSIS-90 pressure and density information we used as an a priori.

3.6.1 Where to start the inversion

As can be seen in Eq. (8) and Eq. (9) the calculation of lidar temperature requires an a priori guess of pressure at the top of the atmosphere and a relative density gradient. Given that the signal to noise in

390   the UMLT can be very low, the choice of a priori as well as the uncertainties in the density gradient can have a very large effect on the temperature profile (Khanna et al., 2011). As a result, it is prudent to remove the top 15 km of the retrieval to minimize the contribution of the a priori (Leblanc et al., 1998b).

In our treatment the a priori pressure is selected at the altitude where the signal to noise ratio in

395   smoothed photon counts profile is 1. The resulting temperature profile is subsequently cut when the relative error exceeds 30 percent. This treatment is not the optimal solution for the retrieval altitude as a fully Bayesian algorithm is required to properly characterize the influence of the a priori choice (Sica and Haefele, 2015). However, we believe that our signal to noise metric is sufficiently rigorous, and more importantly reproducible.

400   ## 4 Net result of temperature algorithm modifications

By implementing the changes from the previous section to both raw data processing and lidar temperature retrieval described in this section we have cooled the UMLT lidar temperature retrievals with respect to the standard NDACC temperature algorithm. This cooling reduces the lidar-satellite warm bias which was noted in the introduction. The modifications cool the mesospheric retrievals

405   by approximately 5 K near 85 km and 20 K by 90 km. There is no significant change to the lidar
temperatures below 70 km.

Figure 11 shows the ensemble median difference between the temperatures produced using the standard NDACC temperature algorithm on LTA data (black), with the modified algorithm (green), the temperatures produced by LiO$_3$S (orange), the satellites MLS (red) and SABER (blue), and
410   the MSIS-90 model (magenta). By implementing the techniques described in the sections above we can account for nearly half of the temperature difference between the lidar and the satellites at 90 km. The character change in the difference functions above and below 84 km is in part due to the increasing contributions of the species specific Rayleigh backscattering correction and the corrections to the gravity vector. The remaining temperature difference between the improved lidar
415   temperatures (green) and the satellites and model may be in part due to distortions in the satellite a priori for the geopotential vector. This possibility is explored further in the companion paper (Wing et al., 2018b).
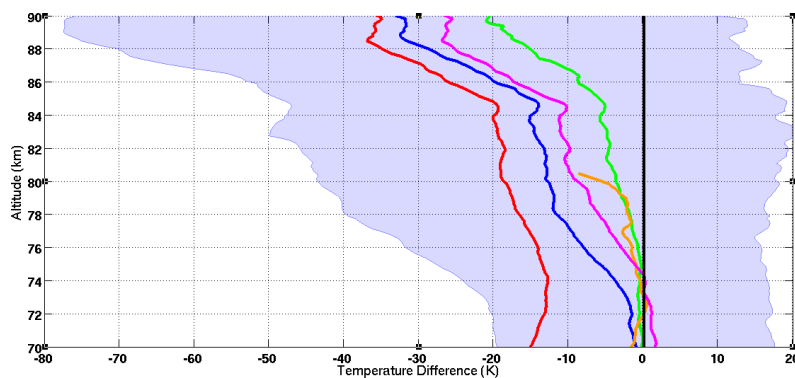
Figure 11: Ensemble temperature differences from NDACC standard LTA Rayleigh temperatures (black). MLS (red), SABER (blue with ensemble variance), MSIS-90 (magenta), LiO$_3$S (orange), and LTA Rayleigh temperatures with corrections given in this work (green).

5   20 Year Comparison of OHP Lidar Temperatures

Conducting systematic inter-comparisons between independent lidar systems is essential for assur-
420   ing data quality and is a requirement for NDACC certified instruments. Most comparisons are conducted on a campaign basis where two or more lidar systems are co-located and make coincident measurements. A good example of this type of work was the stratospheric lidar and Upper Atmospheric Research Satellite (UARS) validation campaign (Singh et al., 1996). This study proposes a completely novel type of inter-lidar study on the long-term stability of the Rayleigh lidar tech-
425   nique. The first step in our analysis is to compare the temperature profiles from the LTA and LiO$_3$S systems. LTA temperatures were calculated using the OHP NDACC temperature code and LiO$_3$S

temperatures were calculated using a modified version of the same code. There are very few significant differences between these two codes. The most important difference involves the choice of parameters for melding the high and low gain channels for the two systems. Given the differences

430 in the relative gain between the four lidar channels being considered, the melding of LiO₃S often occurs at a lower altitude than LTA. This study considers temperatures in between 35 km and 75 km to ensure that we are well above any contamination from aerosols and below any significant initialization errors. From Fig. 11 we can see that there is no significant difference in the temperature outputs of these two algorithms (black baseline and orange) or with the improved algorithm (green)

435 below 75 km.

We selected the data from 1993 to 2013 for the comparison as both instruments operated regularly and without significant design changes during this time. Since the two lidars are co-located and are operated by the same technicians they often make measurements simultaneously. Figure 12 shows the average number of measurements per month made by the LTA and LiO₃S which were included

440 in in this study as well as the average number of common measurements per month. We defined common measurement times based on more than 80% temporal overlap, good quality scans in both systems, and good internal alignment of both lidars. Of the 2482 nights of LTA data and 3194 nights of LiO₃S, 1496 nights met our criteria for coincidence.
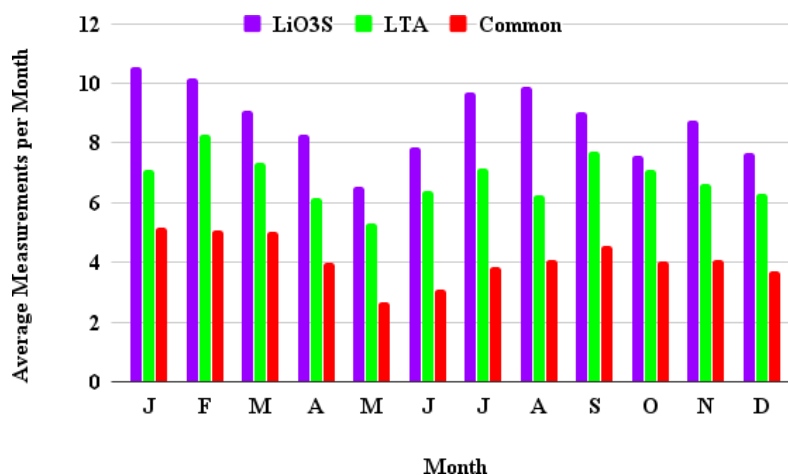
Figure 12: Average number of OHP lidar temperature measurements per month during the period of 1993-2013.

Figure 13 shows the nightly temperature differences between the two lidar systems. The 20 year

445 data set contains 1496 coincident measurements lasting longer than four hours. Black vertical rectangles indicate some of the time periods where the high or low gain channels were mis-aligned in one or the other lidar. A few of these time periods can be associated with minor system modifica-

tions. Misaligned lidar signals were identified by comparing the slopes of the density profiles in the high (generally above 50 km) and low (below ~50 km) gain channels of each system. A simple

450   chi-squared test was used to detect these nights and exclude them from the rest of the analysis.
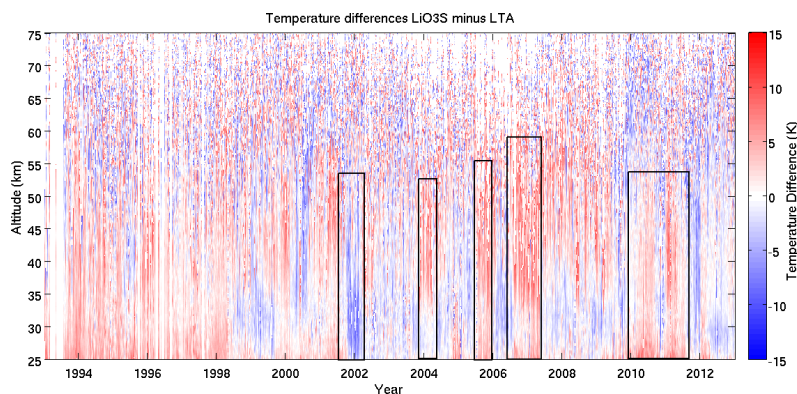
Figure 13: Temperature differences between LTA and LiO₃S OHP lidars for a 20 year period between 1993 and 2013. There are 1496 nights of comparison in this plot. Red indicates that LiO$_3$S was warmer than LTA and blue that it was colder. The black boxes highlight periods where the two lidars were out of alignment with respect to each other.

Figure 14 shows four curves depicting the average temperature differences as a function of altitude and year. The red curve is the average temperature difference between 65 km and 75 km with an average standard deviation of 6.6 K; the green curve is the average temperature difference between 55 km and 65 km with an average standard deviation of 4.5 K; the blue curve is the average

455   temperature difference between 45 km and 55 km with an average standard deviation of 2.7 K; and the magenta curve is the average temperature difference between 35 km and 45 km with an average standard deviation of 1.6 K. Examining the time evolution of the average temperature differences between LTA and LiO$_3$S at four altitude levels gives us confidence that both measurements are stable in both time and altitude. Without excluding misaligned periods (example: winter 2006-2007 in Fig.

460   13 and Fig. 14) the lidar temperature differences are not significant as a function of altitude or year at the 2 sigma level.
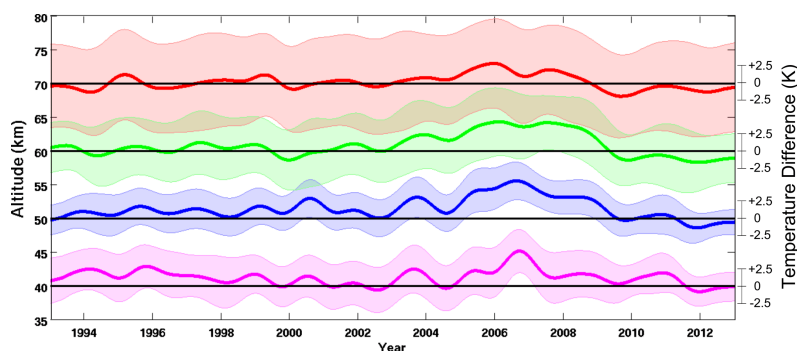
Figure 14: Average temperature differences between LTA and LiO$_3$S OHP lidars for a 20 year period between 1993 and 2013 at four altitude levels: 65-75 km (red), 55-65 km (green), 45-55 km (blue), and 35-45 km (magenta). Shaded uncertainties are shown at 1 sigma for clarity and the black lines are zero temperature difference displaced to 40, 50, 60 and 70 km. All measurements, including periods of lidar misalignment, are included in this plot. The apparent anomalies (e.g. between 2005 and 2009) occur only during times where the lidars were often misaligned, as indicated in Fig. 13.

After removing comparisons between mis-aligned instruments we can calculate the ensemble median difference between the two systems. The ensemble median difference in Fig. 15 shows very good agreement between the two co-located lidar instruments. The temperatures produced by LTA and LiO$_3$S are statistically equal above 45 km for the 20 year period between 1993 and 2013. There is a small –0.6 K systematic difference which reaches a maximum near 40 km. We believe this slight cold bias is due to small differences in the signal melding technique between the high and low gain channels in both systems. On a typical night, the LTA low gain channel starts to significantly contribute to the combined signal near 50 km. If the photon count rate in the low gain channel is too large at these altitudes (due to residual noise contributions or from a slight misalignment with the high channel) the counts will be artificially higher than expected, resulting in a colder temperature. The converse holds true when the low gain channel is misaligned in the opposite sense, resulting in a slight warming due to underestimation of the counts.

The effect of these small temperature perturbations is so small that they can't be seen in single nightly temperature comparisons and were not detected before this study. It is important to note that the 2σ distribution about our ensemble at 40 km has a magnitude of approximately 0.45 K while the statistical error for a single night of lidar measurements near 40 km at 300 m vertical resolution can be on the order of 2 K. Detecting and resolving this small disagreement will be extremely challenging and will not be accomplished in this work.

Given that the primary interest of this work is the upper middle atmosphere (nominally above 50 km), we will focus on the upper portions of Fig. 15 where the two lidars are in statistically perfect agreement. To our knowledge, this is the first ever long-term study of the temperatures produced by

co-located temperature lidars operating at 532 nm and 355 nm. The excellent agreement between these two independent measurements gives us confidence that A) there is no vertical misalignment

485 between the lidars, B) there are no unaccounted for optical transmission effects which influence our temperatures, C) the lidar measurements are accurate and reproducible, D) we can now proceed with some confidence that our ground based lidar measurements can be useful as a calibration source for the space based satellite measurements.
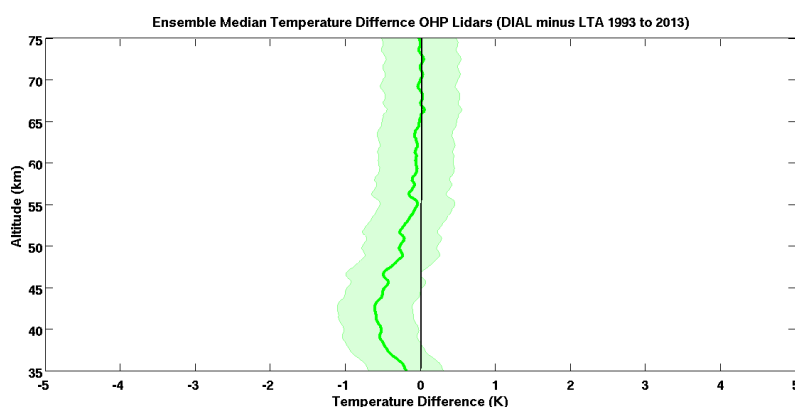
Figure 15: Ensemble of median temperature differences between LTA and LiO$_3$S based on temperature measurements between 1993 and 2013. Shaded error is the two sigma distribution about the ensemble.

6 Summary and Discussion

6.1 Changes to Lidar Temperature Algorithm

490

In this work we have attempted to minimize systematic temperature bias at the top of the lidar temperature retrieval which has been noted previously by several studies cited in the introduction. We have done this by clearly and carefully outlining a rigorous, and complete algorithm for the calculation of lidar temperatures in the UMLT. We have presented techniques for the detection of

495 signal contamination, the selection of the best data for inclusion in the calculation, criteria for where to initialized the inversion when assuming an a priori pressure at the top of the atmosphere, and have demonstrated the benefit of photomultiplier cooling and narrow band pass filters to reduce lidar backgrounds.

After applying our techniques we have seen a systematic cooling of the high altitude lidar tem-

500 peratures which brings them into better agreement with the temperatures measured by both MLS and SABER (Fig. 11). It is also important to note the large variance associated with these ensemble differences can partially be attributed to the lack of control exerted on the error contribution from

the choice of a priori initial pressure for lidar data and a priori contribution and non-LTE effects for
satellite data. Part of the difference may also be due to altitude offsets and coarse vertical resolution.

505   Having applied these new data filtering techniques we have produced an improved lidar tempera-
ture data set which is exploited in the companion paper (Wing et al., 2018b) in an effort to validate
satellite temperatures.

6.2   OHP Lidar 20 Year Comparison

We have conducted the first ever decadal temperature inter comparison between a co-located 532
510 nm Rayleigh lidar and an ozone DIAL system calculating temperatures from a 355 nm line. We
have shown that:

1) Rayleigh lidar temperatures calculated from ozone DIAL non-absorbing 355 nm line are sta-
tistically equal to temperatures from a traditional 532 nm Rayleigh temperature lidar over a large
altitude range. This finding is of particular interest for the NDACC lidar temperature database as
515 temperatures from ozone lidars may also be available for validation and inclusion.

2) Further theoretical work must be done on algorithms for melding data from high and low gain
photon counting channels. The current techniques produce statistically identical nightly temperature
profiles however, a -0.6 K bias near 40 km becomes apparent when multiple years of data are
compared. It is doubtful that current data processing techniques can be easily adapted to address
520 this problem. However, an iterative, cost minimizing, Bayesian approach such as the one proposed
by (Sica and Haefele, 2015) would be able to produce a single melded temperature profile with the
accompanying averaging kernels and an estimate of the error due to the photon count melding. As
a lidar development note, Fig. 13 demonstrates the need move towards the use of automated nightly
alignment of lidar system optics. Manual alignment by operators appears to lack consistency over
525 the time frame of multiple decades.

3) The two independent lidars show no evidence of significant instrument drift over a 20 year
period. This means that ground based lidars are the ideal choice of instrument for detecting small
calibration drifts in satellite remote measurements over long time scales. We rely on this finding to
justify the use of lidars as a reference data set for satellite validation in the companion paper Wing
530 et al. (2018b).

4) There is no evidence of a relative vertical offset between the two independently calibrated
lidar systems which would be seen as an 'S' shaped temperature bias in Fig. 15 due to the sign
change in temperature vertical gradient at the stratopause (Leblanc et al., 1998a). Based on personal
communication, recent July-August 2017 and March 2018 NDACC Ozone validation campaign at
535 OHP (LAVANDE) revealed no vertical shifts between either OHP lidar and the NASA STROZ
mobile validation lidar (McGee et al., 1995).

Acknowledgements. The data used in this paper were obtained as part of the Network for the Detection of Atmospheric Composition Change (NDACC) and are publicly available (see http://www.ndacc.org, http://cds-espri.ipsl.fr/NDACC) as well as from the SABER (see ftp://saber.gats-inc.com) and MLS (see https://mls.jpl.nasa.gov)

540   data centres for the public access via their websites. This work is supported by the project Atmospheric dynamics Research InfraStructure Project (ARISE 2) funded by funded by the European Union's Horizon 2020 research and innovation programme under grant agreement No. 653980 French NDACC activities are supported by Institut National des Sciences de l'Univers/Centre National de la Recherche Scientifique (INSU/CNRS), Université de Versailles Saint-Quentin-en-Yvelines (UVSQ), and Centre National d'Études Spatiales (CNES).

545   The authors would also like to thank the technicians at La Station Géophysique Gérard Mégie at OHP .

References

NDACC Lidar, http://ndacc-lidar.org/.

Alpers, M., Eixmann, R., Fricke-Begemann, C., Gerding, M., and Höffner, J.: Temperature lidar measurements
from 1 to 105 km altitude using resonance, Rayleigh, and Rotational Raman scattering, Atmospheric Chem-
550   istry and Physics, 4, 793–800, doi:10.5194/acp-4-793-2004, https://www.atmos-chem-phys.net/4/793/2004/,
2004.

Apruzese, J. P., Strobel, D. F., and Schoeberl, M. R.: Parameterization of IR cooling in a Middle Atmo-
sphere Dynamics Model: 2. Non-LTE radiative transfer and the globally averaged temperature of the
mesosphere and lower thermosphere, Journal of Geophysical Research: Atmospheres, 89, 4917–4926,
555   doi:10.1029/JD089iD03p04917, http://dx.doi.org/10.1029/JD089iD03p04917, 1984.

Argall, P.: Upper altitude limit for Rayleigh lidar, Annales Geophysicae, 25, 19–25, doi:10.5194/angeo-25-19-
2007, 2007.

Donovan, D. P., Whiteway, J. A., and Carswell, A. I.: Correction for nonlinear photon-counting effects in li-
dar systems, Appl. Opt., 32, 6742–6753, doi:10.1364/AO.32.006742, http://ao.osa.org/abstract.cfm?URI=
560   ao-32-33-6742, 1993.

Dou, X., Li, T., Xu, J., Liu, H.-L., Xue, X., Wang, S., Leblanc, T., McDermid, I. S., Hauchecorne, A., Keckhut,
P., Bencherif, H., Heinselman, C., Steinbrecht, W., Mlynczak, M. G., and Russell, J. M.: Seasonal oscillations
of middle atmosphere temperature observed by Rayleigh lidars and their comparisons with TIMED/SABER
observations, Journal of Geophysical Research: Atmospheres, 114, n/a–n/a, doi:10.1029/2008JD011654,
565   http://dx.doi.org/10.1029/2008JD011654, d20103, 2009.

García-Comas, M., Funke, B., Gardini, A., López-Puertas, M., Jurado-Navarro, A., von Clarmann, T., Stiller,
G., Kiefer, M., Boone, C. D., Leblanc, T., Marshall, B. T., Schwartz, M. J., and Sheese, P. E.: MIPAS
temperature from the stratosphere to the lower thermosphere: Comparison of vM21 with ACE-FTS, MLS,
OSIRIS, SABER, SOFIE and lidar measurements, Atmospheric Measurement Techniques, 7, 3633–3651,
570   doi:10.5194/amt-7-3633-2014, https://www.atmos-meas-tech.net/7/3633/2014/, 2014.

Godin-Beekmann, S., Porteneuve, J., and Garnier, A.: Systematic DIAL lidar monitoring of the stratospheric
ozone vertical distribution at Observatoire de Haute-Provence (43.92°N, 5.71°E), Journal of Environmental
Monitoring, pp. 57–67, doi:10.1039/B205880D, 2003.

Hauchecorne, A. and Chanin, M.-L.: Density and temperature profiles obtained by lidar between 35 and 70
575   km, Geophysical Research Letters, 7, 565–568, doi:10.1029/GL007i008p00565, http://dx.doi.org/10.1029/
GL007i008p00565, 1980.

Keckhut, P., Hauchecorne, A., and Chanin, M.: A critical review of the database acquired for the long-term
surveillance of the middle atmosphere by the French Rayleigh lidars, Journal of Atmospheric and Oceanic
Technology, 10, doi:10.1175/1520-0426(1993)010<0850:ACROTD>2.0.CO;2, 1993.

580   Keckhut, P., McDermid, S., Swart, D., McGee, T., Godin-Beekmann, S., Adriani, A., Barnes, J., Baray, J.-L.,
Bencherif, H., Claude, H., di Sarra, A. G., Fiocco, G., Hansen, G., Hauchecorne, A., Leblanc, T., Lee, C. H.,
Pal, S., Megie, G., Nakane, H., Neuber, R., Steinbrecht, W., and Thayer, J.: Review of ozone and temperature
lidar validations performed within the framework of the Network for the Detection of Stratospheric Change,
J. Environ. Monit., 6, 721–733, doi:10.1039/B404256E, http://dx.doi.org/10.1039/B404256E, 2004.

585 Khanna, J., Sica, R. J., and McElroy, C. T.: Atmospheric temperature retrievals from lidar measurements using techniques of non-linear mathematical inversion, AGU Fall Meeting Abstracts, 2011.

Khanna, J., Bandoro, J., Sica, R. J., and McElroy, C. T.: New technique for retrieval of atmospheric temperature profiles from Rayleigh-scatter lidar measurements using nonlinear inversion, Appl. Opt., 51, 7945–7952, doi:10.1364/AO.51.007945, http://ao.osa.org/abstract.cfm?URI=ao-51-33-7945, 2012.

590 Kumar, V. S., Rao, P. B., and Krishnaiah, M.: Lidar measurements of stratosphere-mesosphere thermal structure at a low latitude: Comparison with satellite data and models, Journal of Geophysical Research: Atmospheres, 108, doi:10.1029/2002JD003029, https://agupubs.onlinelibrary.wiley.com/doi/abs/10.1029/2002JD003029, 2003.

Leblanc, T., McDermid, I. S., Hauchecorne, A., and Keckhut, P.: Evaluation of optimization of lidar temperature

595 analysis algorithms using simulated data, Journal of Geophysical Research: Atmospheres, 103, 6177–6187, doi:10.1029/97JD03494, https://agupubs.onlinelibrary.wiley.com/doi/abs/10.1029/97JD03494, 1998a.

Leblanc, T., McDermid, I. S., Keckhut, P., Hauchecorne, A., She, C. Y., and Krueger, D. A.: Temperature climatology of the middle atmosphere from long-term lidar measurements at middle and low latitudes, Journal of Geophysical Research: Atmospheres, 103, 17 191–17 204, doi:10.1029/98JD01347, http:

600 //dx.doi.org/10.1029/98JD01347, 1998b.

McGee, T. J., Ferrare, R. A., Whiteman, D. N., Butler, J. J., Burris, J. F., and Owens, M. A.: Lidar measurements of stratospheric ozone during the STOIC campaign, Journal of Geophysical Research: Atmospheres, 100, 9255–9262, doi:10.1029/94JD02390, https://agupubs.onlinelibrary.wiley.com/doi/abs/10.1029/94JD02390, 1995.

605 Picone, J. M., Hedin, A. E., Drob, D. P., and Aikin, A. C.: NRLMSISE-00 empirical model of the atmosphere: Statistical comparisons and scientific issues, Journal of Geophysical Research: Space Physics, 107, SIA 15–1–SIA 15–16, doi:10.1029/2002JA009430, https://agupubs.onlinelibrary.wiley.com/doi/abs/10.1029/2002JA009430, 2002.

Remsberg, E. E., Marshall, B. T., Garcia-Comas, M., Krueger, D., Lingenfelser, G. S., Martin-Torres, J.,

610 Mlynczak, M. G., Russell, J. M., Smith, A. K., Zhao, Y., Brown, C., Gordley, L. L., Lopez-Gonzalez, M. J., Lopez-Puertas, M., She, C.-Y., Taylor, M. J., and Thompson, R. E.: Assessment of the quality of the Version 1.07 temperature-versus-pressure profiles of the middle atmosphere from TIMED/SABER, Journal of Geophysical Research: Atmospheres, 113, n/a–n/a, doi:10.1029/2008JD010013, http://dx.doi.org/10.1029/2008JD010013, d17101, 2008.

615 Sica, R. and Haefele, A.: Retrieval of temperature from a multiple-channel Rayleigh-scatter lidar using an optimal estimation method, Appl. Opt., 54, 1872–1889, doi:10.1364/AO.54.001872, http://ao.osa.org/abstract.cfm?URI=ao-54-8-1872, 2015.

Singh, U. N., Keckhut, P., McGee, T. J., Gross, M. R., Hauchecorne, A., Fishbein, E. F., Waters, J. W., Gille, J. C., Roche, A. E., and Russell, J. M.: Stratospheric temperature measurements by two collocated NDSC

620 lidars during UARS validation campaign, Journal of Geophysical Research: Atmospheres, 101, 10 287–10 297, doi:10.1029/96JD00516, http://dx.doi.org/10.1029/96JD00516, 1996.

Sivakumar, V., Prasanth, V. P., Kishore, P., Benchérif, H., and Keckhut, P.: Rayleigh LIDAR and satellite (HALOE, SABER, CHAMP and COSMIC) measurements of stratosphere-mesosphere temperature over a

southern sub-tropical site, Reunion (20.8° S; 55.5° E): climatology and comparison study, Annales Geophys-
625   icae, 29, 649–662, doi:10.5194/angeo-29-649-2011, https://hal.archives-ouvertes.fr/hal-00586264, 2011.

Taori, A., Jayaraman, A., Raghunath, K., and Kamalakar, V.: A new method to derive middle atmospheric
temperature profiles using a combination of Rayleigh lidar and O_2 airglow temperatures measurements,
Annales Geophysicae, 30, 27–32, doi:10.5194/angeo-30-27-2012, 2012.

Taori, A., Kamalakar, V., Raghunath, K., Rao, S., and Russell, J.: Simultaneous Rayleigh lidar and airglow
630   measurements of middle atmospheric waves over low latitudes in India, Journal of Atmospheric and Solar-
Terrestrial Physics, 78-79, 62–69, doi:10.1016/j.jastp.2011.06.012, 2012.

Wing, R., Hauchecorne, A., Godin-Beekman, S., Khaykin, S., and McCullough, E. M.: Lidar temperature series
in the middle atmosphere as a reference data set. Part B: Assessment of temperature observations from
MLS/Aura and SABER/TIMED satellites, Atmospheric Measurement Techniques, Submitted, 2018b.

635   Yue, C., Yang, G., Wang, J., Guan, S., Du, L., Cheng, X., and Yang, Y.: Lidar observations of the middle atmo-
spheric thermal structure over north China and comparisons with TIMED/SABER, Journal of Atmospheric
and Solar-Terrestrial Physics, 120, 80–87, doi:10.1016/j.jastp.2014.08.017, 2014.